Dist: A

REPORT DOCUMENTATION PAGE

Form Approved
OMB No. 0704-0188

1. AGENCY USE ONLY (Leave blank)	2. REPORT DATE	3. REPORT TYPE AND DATES COVERED

4. TITLE AND SUBTITLE

PROCESSING, FABRICATION, CHARACTERIZATION, AND DEVICE DEMONSTRATION OF HIGH TEMPERATURE SUPERCONDUCTING.....

5. FUNDING NUMBERS

F49620-90-C-0079

62301E

7476/01

6. AUTHOR(S)

Dr Thomas S. Luhman

7. PERFORMING ORGANIZATION NAME(S) AND ADDRESS(ES)

Boeing Defense & Space Group
Advanced Research Projects Agency
P.O. Box 3999
Seattle, WA 98124-3707

8. PERFORMING ORGANIZATION REPORT NUMBER

AFOSR-TR- 94 0602

9. SPONSORING/MONITORING AGENCY NAME(S) AND ADDRESS(ES)

AFOSR/NL
110 DUNCAN AVE SUITE B115
BOLLING AFB DC 20332-0001

Maj Erstfeld

10. SPONSORING/MONITORING AGENCY REPORT NUMBER

11. SUPPLEMENTARY NOTES

12a. DISTRIBUTION/AVAILABILITY STATEMENT

Approved for public release;
distribution unlimited

A

12b. DISTRIBUTION CODE

13. ABSTRACT (Maximum 200 words)

A detailed small-angle neutron scattering study of the vortex lattice in a single crystal of YBa2Cu3O7-x was made for a field of 0.5 tesla inclined at angles between 0 and 80 degrees to the crystalline c axis. The vortox lattice is triangular for all angles. For angles less than or equal to 70 degrees its orientation adjusts itself to maximize the pinning energy to densely and highly regularly spaced twin planes. These observations have important implications for the microscopic flux-pinning mechanism, and hence for the critical current achievable in YBa2Cu3O7-x. For large angles (about 80 degrees) the vortex lattice consists of independent chains in the orientation predicted by anisotropic London theory.

472 518

94-31459

14. SUBJECT TERMS

15. NUMBER OF PAGES

16. PRICE CODE

17. SECURITY CLASSIFICATION OF REPORT	18. SECURITY CLASSIFICATION OF THIS PAGE	19. SECURITY CLASSIFICATION OF ABSTRACT	20. LIMITATION OF ABSTRACT
(U)	(U)	(U)	(U)

NSN 7540-01-280-5500

PROCESSING, FABRICATION, CHARACTERIZATION AND DEVICE DEMONSTRATION OF HIGH TEMPERATURE SUPERCONDUCTING CERAMICS

Contract No. F49620-90-C-0079

THIRD QUARTERLY TECHNICAL REPORT

April 30, 1994 - July 30, 1994

Submitted by:

Boeing Defense & Space Group

Sponsored by:

Advanced Research Projects Agency

ARPA Order No. 7476

Monitored by:

AFOSR Under Contract No. F49620-90-C-0079

PM: Dr. Thomas S. Luhman
(206) 773-1991

PI's: Dr. Thomas S. Luhman
(206) 773-1991

Dr. Ilhan A. Aksay
(609) 258-4393

TABLE OF CONTENTS

PROGRAM OBJECTIVE

To develop material pro[illegible]ses and engineering designs for high current applications of $YBa_2Cu_3O_{7-x}$.

PROGRAM DESCRIPTION

The goals of our program are to (1) focus on engineering designs and demonstration of flux-trap magnets; (2) develop improved processing and fabrication methods to enhance current densities in strong magnetic fields; (3) optimize processes for grain alignment in bulk and tape samples; and (4) provide a technology base for utilization of flux-trap magnets.

SUMMARY

a) A detailed small-angle neutron scattering study of the vortex lattice in a single crystal of $YBa_2Cu_3O_{7-x}$ was made for a field of 0.5 tesla inclined at angles between 0 and 80 degrees to the crystalline c axis. The vortex lattice is triangular for all angles. For angles less than or equal to 70 degrees its orientation adjusts itself to maximize the pinning energy to densely and highly regularly spaced twin planes. These observations have important implications for the microscopic flux-pinning mechanism, and hence for the critical current achievable in $YBa_2Cu_3O_{7-x}$. For large angles (about 80 degrees) the vortex lattice consists of independent chains in the orientation predicted by anisotropic London theory.

b) Lower critical field measurements have been performed on two samples of melt grown YBCO prepared under different conditions. Measurements using the ΔM approach were made as a function of temperature both with the field parallel to the c-axis as well as perpendicular to it. Relatively large samples (2-4 mm x 7-9 mm) were used, with regular geometries. The demagnetization question was addressed. 4.2 K Lower Critical Field (LCF) of 920 Oe in the $H\parallel$ orientation and 340 Oe in the $H\perp$ orientation were obtained. LCF temperature dependence was related to the presence or absence, respectively, of optical twinning.

c) Prototype high temperature superconductor flux-trap magnet devices have been used for clamping of a simulated aircraft part during a "live" laser (1500 watt carbon dioxide laser) cut demonstration.

d) A miniature Joule-Thompson cryostat has been assembled with a portable non-magnetic dewar which can house up to a one inch diameter, one fourth inch thick high temperature superconductor single crystal. The unit built to Boeing specifications by R,G.Hansen & Associates of Santa Barbara, California brought a twenty-one gram disk down to below its transition temperature in less than seven minutes. A linear scale-up is possible for superconductors two inches in diameter.

Processing, Fabrication, Characterization and Device Demonstration of High Temperature Superconducting Ceramics: F49620-90-c-0079

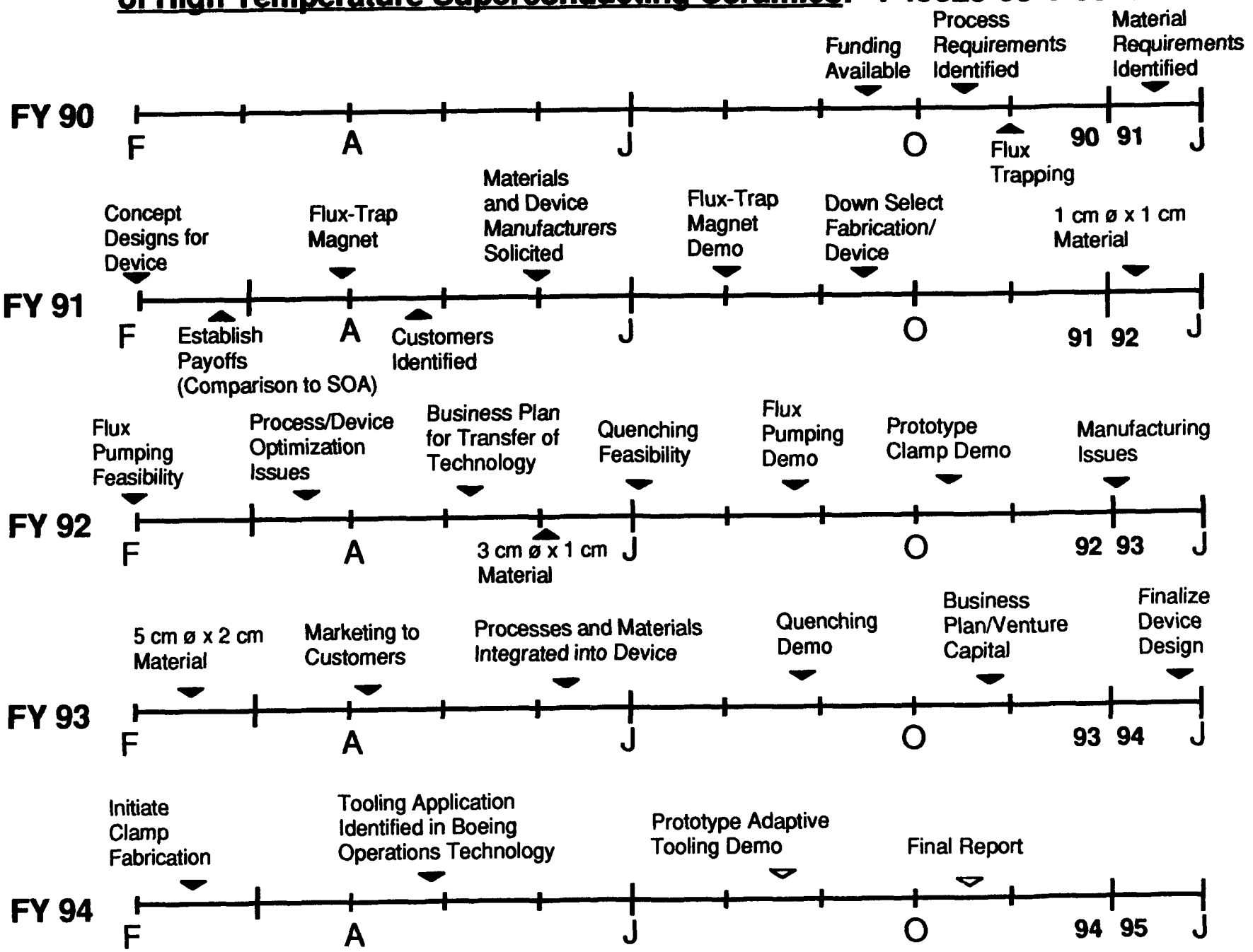

TECHNICAL RESULTS

MATERIALS SYNTHESIS AND CHARACTERIZATION

Inclined-Field Structure, Morphology, and Pinning of The Vortex Lattice in Microtwinned $YBa_2Cu_3O_{7-x}$

The nature of the vortex state in the cuprate high-temperature superconductors remains an issue of great theoretical and practical interest. A variety of experimental techniques have been used to investigate the static dynamic vortex correlations in these materials. In contrast to surface imaging techniques, such as low-field ($B \leq 0.005$ T) Bitter decoration or scanning tunneling microscopy, neutron scattering is sensitive to the entire length of the vortices in the bulk material. Neutron scattering experiments can be performed in a magnetic field range of ~0.05 T up to several teslas, a theoretically interesting regime in which the vortices interact strongly. This is also the relevant field range for prospective magnet applications of the copper oxide superconductors. In fact, the success of our experiments depended critically on the preparation of a large (~2.5-cm diameter, 0.9-cm thickness), high-quality single crystal in a program devoted to device applications of bulk $YBa_2Cu_3O_{7-x}$.

The experiments address two interrelated issues. First, the layered structure of the copper oxides and the concomitant large anisotropy of the electronic properties give rise to complex current and field distributions around individual vortices. The ensuing unusual interactions between vortices can lead to novel vortex structures as the magnetic field is inclined at an angle Θ with respect to the c axis. By performing neutron experiments for $0° \leq \Theta \leq 80°$, we tested these theories in fields up to 0.5 T. A second issue of great practical significance is the interaction of the vortex lattice with pinning centers that prevent dissipative vortex motion at high temperatures and cause flux trapping as the external field is removed. We carried out extensive electron microscopy studies to identify the microstructural features potentially responsible for flux pinning in our samples. Our neutron measurements indicate that among the possible candidates (inclusions of the nonsuperconducting Y_2BaCuO_5 phase, stacking faults, and twin planes) only the densely spaced twin planes have a substantial effect on the structure of the vortex lattice.Prior evidence for the importance of twin planes as pinning sites derives mainly from Bitter decoration and transport studies conducted for either $\Theta = 0°$ or $\Theta = 90°$. We show that the vortex lattice orientation locks into the orientation of the twin planes up to a surprisingly large inclination angle $\Theta \approx 70°$. We discuss this observation in terms of microscopic models of the vortex structure. For larger inclination angles, we report the observation of a vortex chain state.

The single-crystal sample was synthesized by a seeding technique in a temperature gradient. The characterization of our sample by transmission electron microscopy was carried out by the cutting of several sections perpendicular to the (001) and (110) planes from an identically prepared crystal. A selected-area diffraction pattern with the electron beam in the (001) direction is shown in Fig. 1. The orthorhombic strain $\Delta a = (b_o - a_o) / a_t = 1.8\%$ (a_o , b_o , a_t are the basal-plane lattice parameters in the orthorhombic and tetragonal phases) determined from the splitting of the [110] diffraction peak is identical for several sections of the sample. The strain created as the sample is cooled through the tetragonal-orthorhombic transition at 700°C is relieved by the formation of two variants of twin boundaries. As discussed previously, the separation D of the twin boundaries is inversely proportional to Δa, so the highly regular twin-plane spacing again indicates a homogenous distribution of oxygen. By measuring 250 twin domains we obtained $D = 900 \pm 30$ Å. We determined the width of the twin boundaries to be 15 ± 5 Å from the width of the weak rod of scattering extending in the direction around the diffraction peak of Fig 1. Because this width is of the order of in-plane superconducting coherence length, the twin planes may be effective core-pinning sites.

Electron micrograph showing one family of twin boundaries in one of our crystals. The inset is a selected area diffraction pattern showing the orthorhombic splitting of the [h00] Bragg reflections. From the uniformity of the orthorhombic splitting for different sections of the sample, a highly homogeneous distribution of oxygen throughout the sample can be deduced.

Fig. 1

Our coordinate system is defined in Fig.2. The angles $\varkappa$ and ϕ are determined by the orientation of the crystal by x-ray diffraction outside the cryostat. Once the sample is mounted in the cryostat, the angles θ and ϑ can be changed by the rotation of either the cryostat inside the magnet or the entire cryostat-magnet assembly, respectively. The crystalline (100) axis in the (x,y) plane to ±3°, so that $\phi \approx 45°$. We performed the neutron scattering experiments for two different values of $\varkappa$: 0° ± 1° and 9° ± 1°. It is important to understand the difference between these two configurations: In the first case, the magnetic field bisects the angle between the two sets of twin planes for any value of θ. In the second case, the c axis is slightly offset from the field direction by $\varkappa = 9°$ at $\theta = 0°$, so that for $\theta \neq 0°$ the angles $\alpha_\pm$ subtended between the magnetic field and the two sets of twin planes. This small difference in angle has profound consequences for the structure of the vortex lattice.
The data for $\varkappa = 0°$ and $\varkappa = 9°$ are shown Fig.3, A to F, and Fig.3, G to I, respectively. For $\theta = \varkappa = 0°$, we observe the diffraction pattern with fourfold symmetry reported for both zero and nonzero ϑ. This result led others to the conclusion that the vortices for a square lattice, which maximizes the binding energy between vortices and both sets of twin planes, rather the triangular lattice expected if vortex-vortex interactions dominate. To investigate this point further we oriented the crystal so that $\varkappa = 9°$ and $\theta = 5°$ (Fig.3G). This small angular offset causes a single-domain triangular lattice to be formed in the entire crystal, as evidenced by the hexagonal diffraction pattern. A fit to the circularly averaged intensity profile gave a peak position (τ) of 0.0092 ± 0.003 $Å^{-1}$, somewhat smaller than the value of $\tau = 2.15\pi\sqrt{B}\,\Phi_0 = 0.0105$ $Å^{-1}$ calculated from the flux quantization rule for an undistorted triangular lattice (Φ_0 is the flux quantum. Within experimental error, no such expansion of the average lattice spacing is observed for a larger θ. The slight expansion of the $\theta \approx 0°$, together with the significant transverse broadening of four of the reflections, indicates the formation of defects that lead to an accumulation of vortices near twin planes.

Because of the poor longitudinal resolution of our instrument, we can only put a lower bound of ~3 lattice spacings on the translational correlation length. The instrumental resolution in the ϑ direction is much sharper (~0.2°), and rocking curves in the ϑ direction revealed an intrinsic width of $\Delta\vartheta \approx 1°$ for the Bragg reflections, in agreement with previous measurements. The correlation length ξ^* of the vortex displacement field in the magnetic field direction is given approximately by $\xi^* = (\tau\Delta\vartheta)^{-1} \approx$ 6000 Å. The vortices are therefore significantly deflected from the field direction as they bend and follow the twin plane over some distance to gain advantage of the twin-plane pinning energy. In this model, the finite-range order in the twin-plane position.

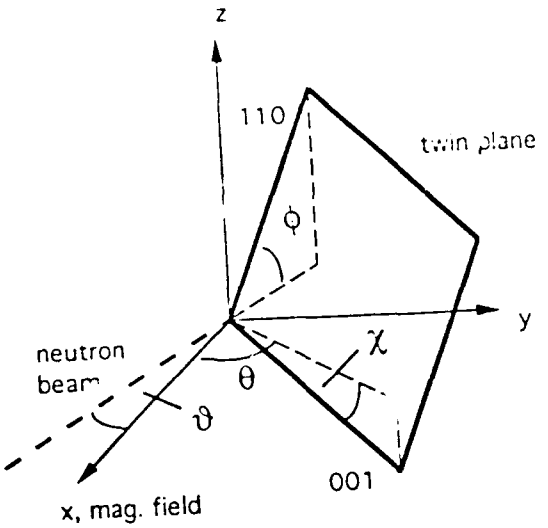

Coordinate system defining angle conventions. Experiments were carried out with χ fixed at either 0° or 9°, ϕ fixed at 45°, and θ and ϑ varied. The coordinates y and z perpendicular to the magnetic field (x axis) are the abscissa and ordinate, respectively, the diffraction patterns shown below.

Fig.2

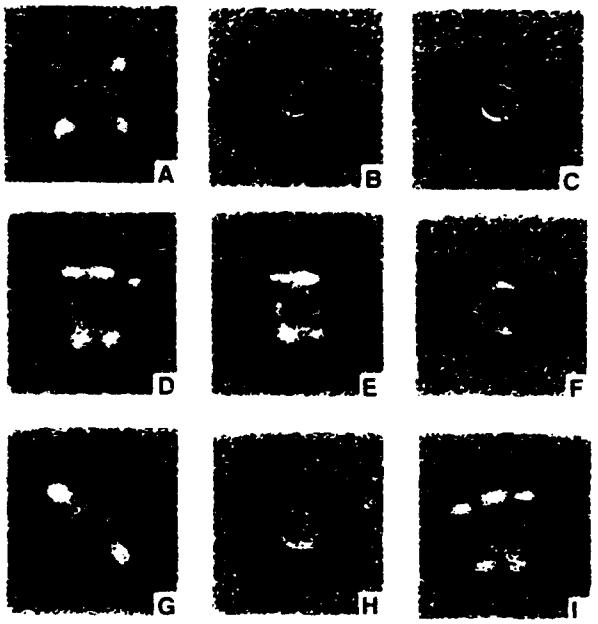

Small angle neutron diffraction patterns obtained from our $YBa_2Cu_3O_7$ single crystals at the NIST 30m SANS spectrometer. The angle θ between the crystalline c-axis and the magnetic field direction is varied such that A) $\theta = 0°$, B) $\theta = 50°$, C) $\theta = 60°$, E) $\theta = 70°$, F) $\theta = 80°$, G) $\theta = 5°$, H) $\theta = 30°$, I) $\theta = 60°$. For panels A-F the angles between the magnetic field and both sets of twin planes are equal, while for panels G-I the angles are different. From

Fig.3

The vortex line tension, which opposes this bending, leads to the formation of a single-domain pattern (Fig.3G): The lowest elastic energy and maximum pinning energy of the vortex lattice are achieved if the orientation of one of the principal axes is given by the set of twin planes subtending the smaller angle α with respect to the magnetic field. The square pattern of Fig.3A arises simply as a superposition of two orientations that are degenerate for $\alpha = 0°$.

The broadening of the θ rocking curves persists up to $\theta \sim 40°$. However, for $\theta \geq 50°$ the reflections become resolution-limited in all directions. These results are qualitatively consistent with high-temperature transport measurements revealing a drop in the resistivity due to vortex motion when the critical field is applied within a "critical angle" width respect to the twin planes. It has been suggested that vortex bending becomes energetically unfavorable above this critical angle; our neutron scattering data provide microscopic evidence for such behavior. Inspection of the diffraction patterns of Fig.3, B to E, reveals that although the distortion of the vortex is consistent with equations, the orientation of the lattice does not follow the prediction of the effective mass model because no reflection with a zero y component (Fig.2) is observed. For a small θ, the orientation of the vortex lattice is determined by pinning interactions between vortices and twin planes. Therefore, we postulate that this relation remains true for a larger θ, which leads to a quandary. The correlation length of the displacement field along the magnetic field direction, for $\theta \geq 50°$, is resolution -limited and therefore at least ~2 μm. Hence, any bending of the vortex induced by the twin planes must be allowed to "heal" on a length scale shorter than the twin-plane spacing so that this bending does not cause a long-range displacement field reflecting the imperfect twin-plane periodicity. If, on the other hand, the vortex is assumed to be microscopically homogeneous, the pinning energy should not depend on the location of the intersection point between the vortex and the twin plane.

A length scale much shorter than the twin-plane spacing naturally arises in microscopic models of the vortex structure that also take the discreteness of the crystalline layer structure into account. In such models the vortex consists of "pancake" vortices in the ab plane separated by interplanar Josephson vortices. It has been argued that the pinning forces experienced by the Josephson segments are reduced by a factor of $(\epsilon\xi/d)^3$ with respect to the force experienced by pancake vortices. For $YBa_2Cu_3O_{7-x}$, the in-plane coherence length $\xi \sim 15$ Å and the interlayer spacing is $d \sim 10$ Å, so that we can neglect the pinning force on the interlayer segments and concentrate on the pinning forces on the pancakes. The pinning energy of the pancake

vortices is maximized when one of the principal axes of this lattice is parallel to the "picket fence" pattern of twin boundaries. Viewed along the field direction, the reciprocal lattice vectors of the rotated lattice in the two twin-plane domains allowed us to carry out a detailed quantitative analysis of the peak positions. The radial peak positions were obtained from fits to sector averages and were found to be in quantitative agreement for $\theta \leq 60°$. Three dimensional Three-dimensional corrections apply for $\theta \geq 70°$. To obtain the angular peak positions, we averaged the data radially in an elliptical annulus of appropriate eccentricity. Fig. 4 shows the typical results of this procedure, together with the predictions from calculated values. Except for the unexplained asymmetry of a few reflections,, the observed peak positions are in substantial agreement. This agreement validates our simple model and necessitates an essentially two-dimensional flux pinning mechanism. Finally, we focus on the diffraction pattern for $\theta = 80°$ (Fig.3F), which is inconsistent with calculated values. In fact, the anisotropic London model predicts the position of these reflections correctly. A reorientation of the vortex lattice into the unique orientation predicted by anisotropic London theory is expected for a large θ. Fits to high-quality diffraction patterns for B of 0.535 T, θ of 77°, and neutron wavelengths (χ) of 6 and 10 Å yield a value of 0.0061 ± 0.0003 $Å^{-1}$ for the radial peak position. The corresponding $\epsilon = 0.23 \pm 0.05$ is within the errors consistent with the values extracted from Bitter decoration patterns.

For a large θ, the triangular vortex lattice is severely stretched in the direction perpendicular to both B and c and can be regarded as a collection of chains whose periodicities are locked. Anisotropic London theory predicts an attractive double well in the intervortex interaction along the chains for small fields, so that the vortices should penetrate as independent chains for small fields, so that the vortices should penetrate as independent chains as the field is increased through the lower critical field H_{c1}. Such a vortex chain state has been observed in low-field Bitter decoration in $YBa_2Cu_3O_{7-x}$. Some workers have used the same theory to predict the persistence of this vortex-lattice shear modulus corresponding to translations of the chains in the chain direction. In $YBa_2Cu_3O_{7-x}$ for B = 0.5 T, the chains are predicted to decouple for $\theta \geq 80°$, thus giving rise to a diffraction pattern consisting of just two reflections. The data represented in Fig.3F confirms this prediction. By translating the detector with respect to the beam to probe a wider momentum range and taking diffraction patterns for different values of θ, we observed only broad and weak diffuse scattering around the remaining four reciprocal lattice vectors for fields of 0.1 and 0.5 T. The broadening of these Bragg peaks reflects the loss of long-range order in the direction perpendicular to the chains. In contrast to observations in other anisotropic superconductors,

but in agreement with observations in $YBa_2Cu_3O_{7-x}$ at low fields, we therefore conclude that the mean field anisotropic London theory provides an adequate description of the structure and orientation of the vortex lattice in this material. However, we have also shown that pinning to correlated microstructural defects can obliterate this intrinsic behavior and lead to unexpected changes in morphology and orientation of the vortex lattice as a function of θ. It will be interesting to extend this investigation into a temperature and field range in which the melting of the flux-line lattice is expected to occur. For device applications, the strong response of the vortex lattice to the presence of twin planes, and the absence of any measurable influence of any other microstructural feature, makes the structural design and configuration of twin planes a promising approach to enhance the flux-trapping properties of these materials.

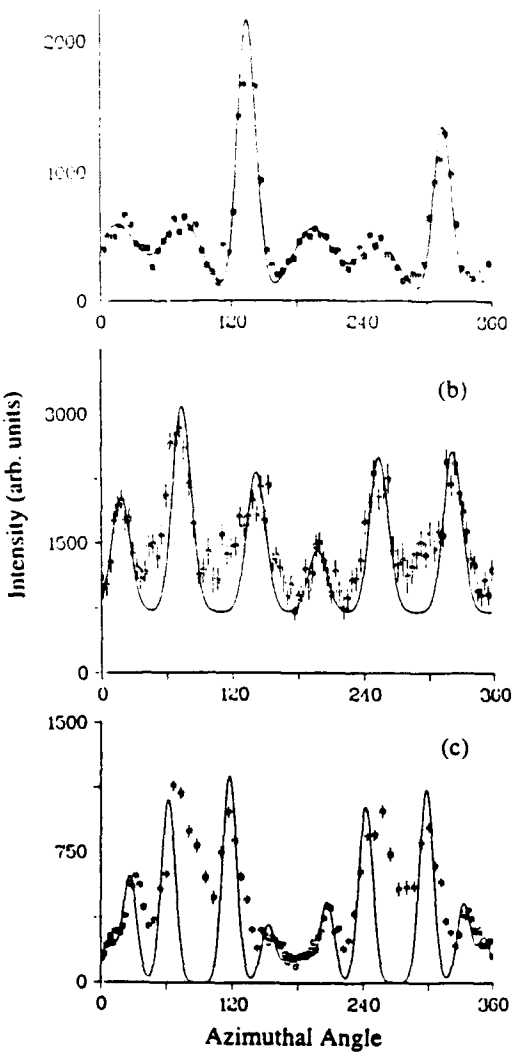

Diffraction patterns for (A) $\chi = 0°$, $\theta = 5°$, (B) $\chi = 9°$, $\theta = 30°$, (C) $\chi = 0°$, $\theta = 5°$, radially averaged over an elliptical annulus of 15 to 20 pixels in width. The azimuthal angle is the angle subtended by a ray from the origin to the center of the annulus and the positive y axis. (A) and (B) show six reflections corresponding to a single-domain vortex lattice. In (C) the Bragg condition is satisfied only for eight of the twelve reflections of the domain lattice. The solid lines show the predicted peak positions. The relative peak heights carry no meaning (the intensity units are arbitrary).

Fig.4

Lower Critical Field Studies of Melt-Textured and Melt-Grown $YBa_2Cu_3O_{7-x}$

Numerous methods for measuring the lower critical field, LCF or H_{c1}, of high-T_c superconductors have been utilized. The methods used are based on: (i) magnetization measurement, (ii) magnetic screening, (iii) radio frequency techniques, (iv) torque and mechanical oscillation, (v) muon and spin resonance, and (vi) optical visualization of magnetic flux. A Method of LCF determination derived from an extended Bean model, relies on the existence of a trapped magnetization, M_t, that is proportional to an $(H-H_c)^2$. A plot of $\sqrt{M_t}$ versus this H extrapolates to H_{c1}. An advantage of the method is that it is based on a relatively large data set rather than the usual detection of the departure of a single point from the Meissner line. Likewise a "hysteritic method" for superconducting cylinders, also based on the Bean model, enables an H_{c1} to be extracted from an extensive set of hysteritic-loss versus sweep-amplitude data taken above H_{c1}. The application of this method to two samples (designated "CPS3"and "CPS4"), independently produced by similar techniques, yielded LCF's of 163 and 162 Oe, respectively. Another sample of melt textured YBCO (designated "DC1") yielded 225 Oe.

In melt texturization a molten zone is made to pass along a rod of compacted YBCO. The fast-growing a-b planes tend to lie parallel to the growth direction (the rod axis), causing the c-axes of the resulting crystallites to be randomly directed but always normal to the rod axis.

Further investigation of the LCF was logically chosen to be upon carefully oriented single crystals of YBCO.

Two large crystals of $YBa_2Cu_3O_{7-x}$ were prepared by variants of the melt-growth technique pioneered by Murakami et al. Crystal A was grown using a modified Bridgman technique from a $SmBa_2Cu_3O_{7-x}$ seed (oriented with the a-b-plane parallel to the large surface) previously imbedded in a sintered YBCO bar.

Sample A, in the form of a square prism 2.26 x 2.85 x 9.34 mm^3, was removed from this crystal and oxygenated for 48h/500°C plus 24h/400°C. The c-axis was perpendicular to one of the long faces of the prism. Crystal B was grown at 1050-1080°C in air (from a $SmBa_2Cu_3O_{7-x}$ seed oriented with the a-b plane parallel to the upper surface). The crystal was oxygenated for 168h/450°C after sample B, in the form of a cylinder 4.82 mm^{ϕ} x 7.06 $mm^{\perp}$, was removed from it using a hollow-core diamond drill. The c-axis was parallel to the cylinder axis. Magnetization measurements were carried out in a vibrating-sample magnetometer operating with a 17 kOe iron-core electromagnet. Sample A was measured with the field in a plane perpendicular to the long axis. With sample B the field was perpendicular to the cylinder axis.

After cooling the sample in zero field, initial magnetization measurements were performed on both samples as function of temperature from 4.2 K to T_c. A straight line was then subtracted from the data and an LCF (uncorrected for demagnetization) was then taken as the field associated with the first nonzero value of magnetization-difference, ΔM; see Figs.5&6. Demagnetization factors, n, were determined from the slope of the initial-magnetization straight line using $\chi = -1/(4\pi(1-n))$; they were seen to agree with the ellipsoidal approximation to better than 10%. The demagnetization-corrected LCF is then given by $H_{c1} = H_{\bullet} / (1-n)$, Where $H_{\bullet}$ is the applied field for first flux entry (i.e. the uncorrected LCF).

Sample A: Measurements were made on sample A both with the field along the c-axis ($H\|$) and perpendicular to it ($H\perp$). The results, corrected using an $n\|$ of 0.466 and an $n\perp$ of 0.502, respectively, are shown in Fig. X. Taking the $H\|$ results first, we note that the 4.2 K value of 920 Oe is close to the literature average, Table 1. On the other hand, the 4.2 K $H\perp$ value of 430 Oe is rather high, and consequently the resulting $A = H\|/ H\perp$ is considerably lower than average. See Fig. 5.

Sample B: With sample B the c-axis was along the cylinder axis, making the geometry amenable to a calculation of the demagnetization factor for the field-traverse case (yielding $n\perp$ = 0.410) and hence for the measurement of $H\perp$. In this case we made the ellipsoidal approximation, which should be valid since the weaker shielding currents are flowing along the length of the cylinder, where the largest fields exist, and the conventional demagnetization correction applies. The data are presented in Fig. 6, where we see a 4.2 K $H\perp$ of 340 Oe, which although higher than most of the literature data, is not outside its range.

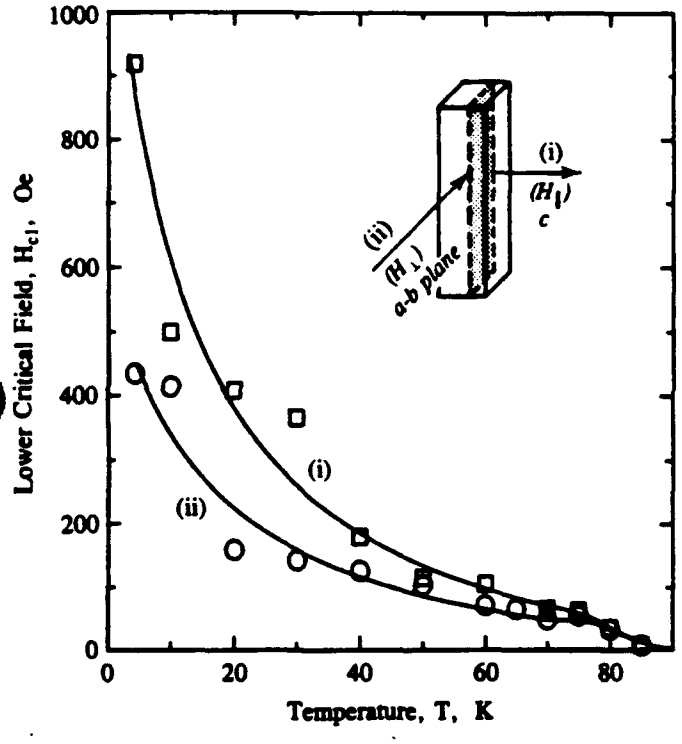

Fig. 5: H_{c1} *versus* T for Sample A in the $H_{\parallel}$ (i) and the $H_{\perp}$ (ii) orientations, both corrected for demagnetization.

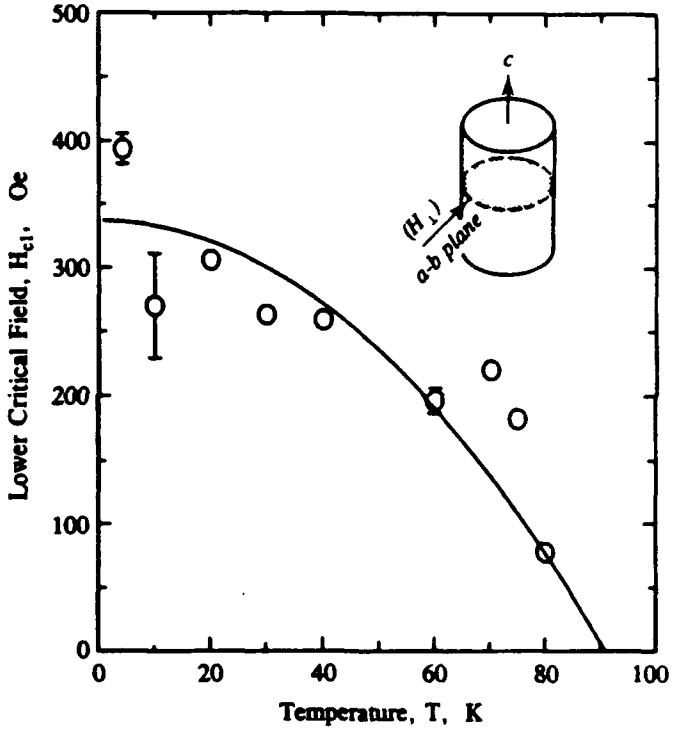

Fig. 6: H_{c1} *versus* T for Sample B in the $H_{\perp}$ orientation, corrected for demagnetization.

SUPERCONDUCTIVE DEVICE REQUIREMENTS AND DESIGNS

Prototype High Temperature Superconductor Clamps in Operation

Fig. 7 shows a 1500 watt carbon dioxide industrial laser with a Boeing 737 tool for cutting out stainless steel cockpit cabin window reinforcement panels. The strengthening parts are to be placed inboard of the outer-skin peripheral to the aircraft flight control area. The normal practice for holding the metal panel to the tool during laser cutting is with either shop-vacuum or cleco clamps. Shop-vacuum has proven difficult to work with because of its low holding force. In addition the part must mate well with the tool for the procedure to work at all. When cleco clamps are used to hold the part to be cut to the tool, tabs must be provided around the border of the part. These tabs have to be removed in a separate operation to finish the part. Figs. 8 & 9 show a part that has just been cut after being held in place by two self contained high temperature superconductor clamps. The portable devices contain a supply of onboard liquid nitrogen. In addition handles can be seen which allow a high-permeability magnetic flux enhancer core to be inserted into and out of a single crystal superconductor ring within the device, greatly amplifying the clamping force. In other tooling configurations the superconductor magnet clamps could be built into the base of the tool itself. Additionally a matrix of small diameter superconductor clamps could hydraulically raise or lower, and gimbal to adapt to the topological requirements of any part at hand.

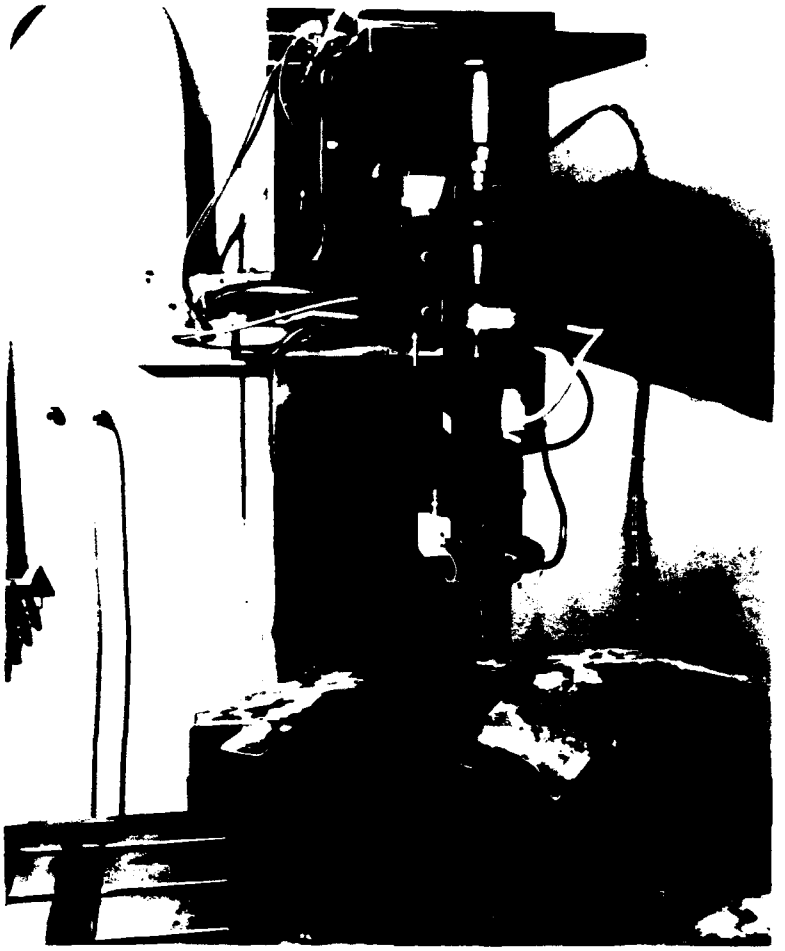

1500 watt carbon dioxide industrial laser, with a Boeing 737 tool for cutting out stainless steel cockpit cabin window reinforcement panels.

Fig.7

A part that is being held in place during a laser cut operation.

Fig.8

A laser cut part just after removal of flux-trap superconductor clamps.

Fig.9

High-Temperature Superconductor Joule-Thompson-Cryostat Clamp Device

Boeing, working in collaboration with R.G.Hansen & Associates of Santa Barbara, California have devised a high temperature superconductor clamp (Fig. 10), which allows a one inch diameter disk weighing 21 grams to cool from ambient to 77.9 K in just over 6 minutes. The clamp is cooled by a miniature Joule-Thompson cryostat powered by high-pressure high-purity nitrogen gas. The nitrogen gas is supplied via a small diameter stainless steel feed tube visible as a dark line exiting the rear of the device (on the display stand in Figs. 10 & 11). Connected to a reservoir of pressurized gas a whole battery of superconducting clamps could all be powered at once, such as for adaptive tooling applications. For completely portable operation a small gas bottle can be fitted directly to the cryostat clamp assembly (Fig. 12). Such clamp systems can be operated in any attitude or position, including upside-down.

To turn the clamp devices off one need merely to either shut-off the gas supply or suddenly reduce its pressure with an expansion valve. With the gas supply turned off the flux-trap superconductor will slowly warm to above its transition temperature of 91 K (≈1-4 minutes, depending on the heat-loss characteristics of the specific device), and the magnetic field will collapse as the supercurrents cease. The cryostat can then be feed somewhat lower pressure nitrogen gas to allow the device to remain in the "ready" mode. This procedure will greatly reduce the time required for the next cool-down period, and will minimize the thermal shock to the ceramic superconductor by maintaining a very low ΔT during cycling. An alternate method of warming the superconductor would be to rapidly drop the pressure to the cryostat via a expansion valve configured into the device. Then by utilizing the reverse Joule-Thompson effect, heat is released directly at the cold-finger assembly (upon which the superconductor specimen is mounted: Fig.11).

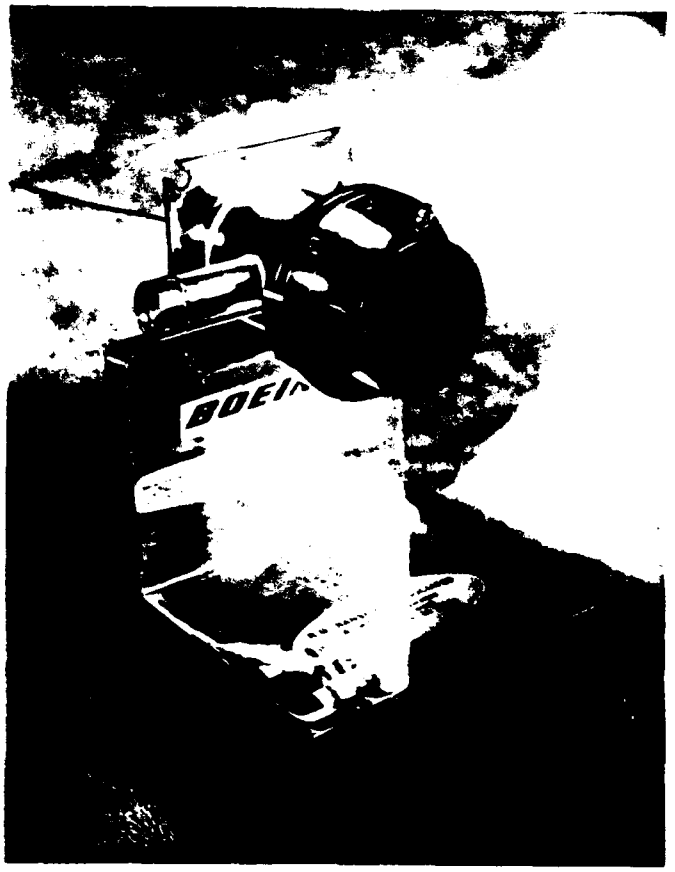

A high temperature superconductor clamp with Joule-Thompson cryostat.

Fig. 10

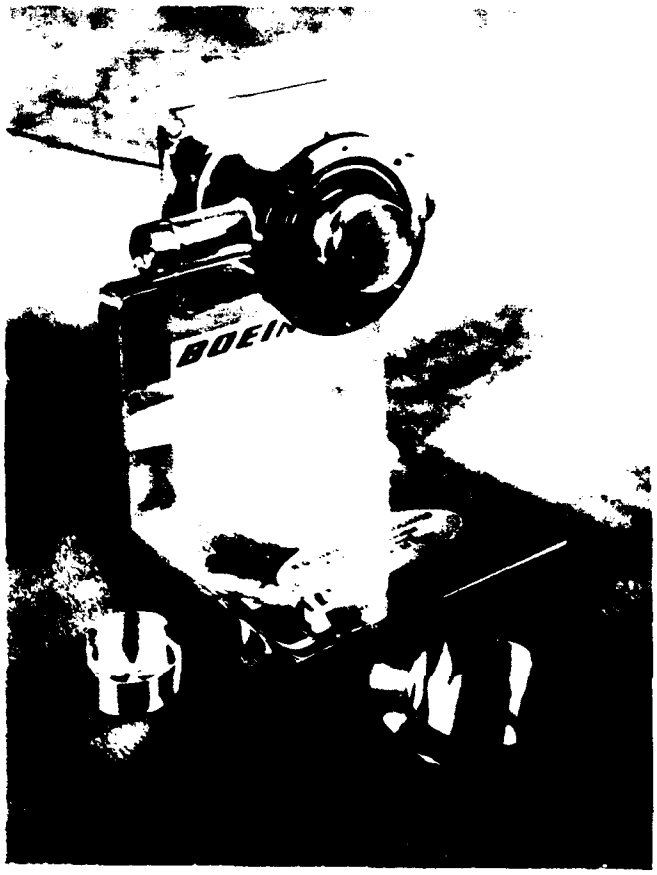

Disassembled superconductor clamp mounted on display stand, showing 1" diameter superconductor disk in left foreground.

Fig.11

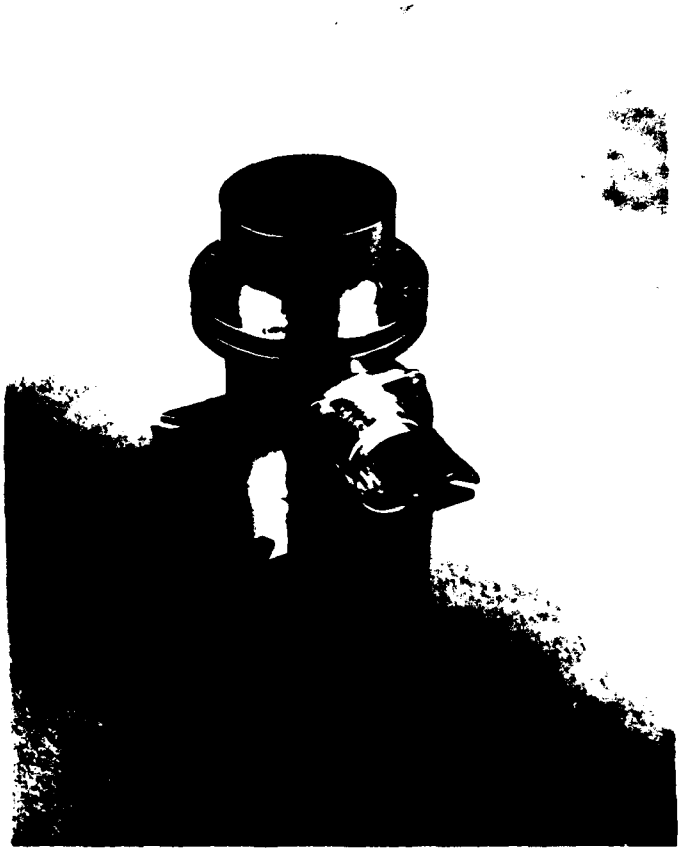

Integral superconductor clamp, Joule-Thompson cryostat, liquid nitrogen dewar assembly.

Fig. 12